BIFURCATIONS OF NATURAL CONVECTION FLOWS FROM AN ENCLOSED CYLINDRICAL HEAT SOURCE

Diego Angeli[a,*], Arturo Pagano[b], Mauro A. Corticelli[a], Alberto Fichera[b], Giovanni S. Barozzi[a]

[a]DIMeC - Dipartimento di Ingegneria Meccanica e Civile, Università di Modena e Reggio Emilia, Via Vignolese, 905, I-41125, Modena (MO), Italy
[b]DIIM - Dipartimento di Ingegneria Industriale e Meccanica, Università degli Studi di Catania, Viale Andrea Doria, 6, I-95125 Catania (CT), Italy

ABSTRACT

A numerical analysis of transitional natural convection from a confined thermal source is presented. The system considered is an air-filled, square-sectioned 2D enclosure containing a horizontal heated cylinder. The resulting flow is investigated with respect to the variation of the Rayleigh number, for three values of the aspect ratio A. The first bifurcation of the low-Ra fixed-point solution is tracked for each A-value. Chaotic flow features are detailed for the case A = 2.5. The supercritical behaviour of the system is investigated using nonlinear analysis tools and phase-space representations, and the effect of the flow on heat transfer is discussed.

Keywords: *Buoyancy-induced flows, Horizontal cylinder, Transition, Bifurcations, Heat transfer.*

1. INTRODUCTION

Natural convection from enclosed thermal sources has been studied extensively, due to its importance in a variety of technological applications. A major part of the relevant literature focuses on heat transfer performances (Warrington and Powe, 1985), and the most significant results are summarized in heat transfer handbooks (Hewitt, 1992; Bejan, 2004).

Comparatively few works dealt with the onset of complex and time-dependent regimes (Desrayaud and Lauriat, 1998). Nevertheless, from a theoretical and practical standpoint, the interest in this topic is growing continuously, since a large variety of flow structures can be observed for different geometrical and thermal configurations. The characters of the flow regimes are expected, in turn, to affect heat transfer both locally and globally.

The system considered here is sketched in Fig. 1. A horizontal cylinder of diameter D, is centred in a cavity of square cross section, filled with air at $Pr = 0.7$. The z-axis of the coordinate system coincides with the cylinder longitudinal axis, while the y-axis is parallel and opposed to the gravitational field. The cavity extension along z is assumed to prevail over L, the cavity side length; therefore, the physical three-dimensional system is reduced to its 2D transversal square section. Attention is thereby restricted to the (x, y) plane in Fig. 1. The temperature of the enclosure walls is uniform, $T = T_W$; the cylindrical source is treated as isothermal as well, $T = T_S$, with $T_S > T_W$. The buoyancy-induced flow regimes are investigated with respect to the variation of the Rayleigh number, Ra_H, based on the gap width H. The aspect ratio of the system, A, is defined as the ratio between the cavity side length L and the gap H, $A = L/H$.

The onset of transitional and time-dependent flow regimes arising from enclosed heat sources has been extensively considered for the cylindrical annular configuration (Angeli *et al.*, 2010), and a large amount of experimental data has been collected on that geometry (Teertstra and Yovanovich, 1998). Due to its simplicity, several analytical solutions for steady-state are also available (Mack and Bishop, 1968; Desrayaud *et al.*, 2006), as well as theoretical studies concerning the stability of the system (Mojtabi and Caltagirone, 1979). The geometry considered here has gained much less attention. In this context, the most outstanding contribution was given by Desrayaud and Lauriat (1998), who thoroughly investigated horizontal line heat sources immersed in air-filled rectangular vessels.

Recently, for the configuration addressed herein, Angeli *et al.* (2008) predicted numerically a number of transitional phenomena, for values of the aspect ratio A ranging between $A = 2.5$ and $A = 5$. A first estimate of a critical Ra_H-value, $Ra_H = 2 \times 10^4$, was also provided, valid for all the A-values. A more detailed analysis of such transitions is presented in this work. Predictions of the asymptotic flows are performed via a 2D finite-volume simulation code, specifically developed for the analysis of natural convection regimes. The governing equations are solved on Cartesian grids, and the presence of non-aligned boundaries is taken into account by introducing appropriate corrective terms in the discretized equations (Barozzi *et al.*, 2004).

Computations are carried out for three values of the aspect ratio A, namely $A = 2.5, 3.\bar{3}, 5$. For each A-value, early bifurcations of the low-Ra fixed point solution are followed for increasing Ra_H, until either unsteady or non-symmetric flows are encountered. Limitedly to the case $A = 2.5$, successive transitions of the supercritical flow pattern are tracked by a number of long term, high-Ra simulations. To this aim, time series of the dependent variables (velocity components and temper-

---

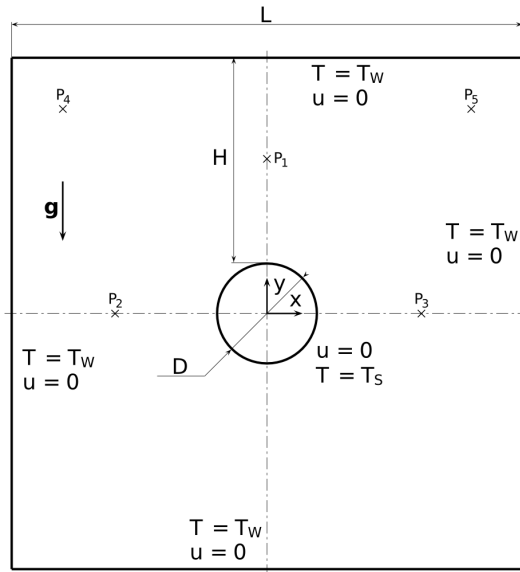*Corresponding author. Email: diego.angeli@unimore.it

Fig. 1 Schematic of the system under consideration; ($\times$) symbols indicate locations of the sampling points placed across the cavity.

ature), are extracted in 5 locations evenly scattered over the cavity, as represented in Fig. 1. The occurrence of complex non-linear dynamics is identified by means of phase-space representations and power spectra of the computed time series.

2. METHODOLOGICAL ASPECTS

The problem is stated in terms of the incompressible Navier-Stokes formulation. The Oberbeck-Boussinesq approximation is enforced, all the fluid properties being consistently assumed as constant, apart from density in the buoyancy term.

The governing equations are tackled in their non-dimensional form. Angeli *et al.* (2008) indicate the gap between the top of the cylinder and the upper cavity wall as the most suitable scale length, $H_{ref} = H$, for it reduces the dependence of the solution ranges on the aspect ratio (in particular for what concerns the heat transfer rate and the first transitions between different regimes). Moreover, the region above the cylinder is subject to the maximum inverse thermal gradient, *i.e.* to the highest buoyancy force acting on the fluid system, and this is again related to the reference length H.

Temperature is non-dimensionalized according to the temperature difference between the cylinder and the cavity walls ($T_{ref} = T_S - T_W$), and the following velocity scale is chosen:

$$U_{ref} = \sqrt{g\beta T_{ref} H_{ref}} \qquad (1)$$

The continuity, momentum, and energy equations are given the following form:

$$\nabla \cdot \tilde{\mathbf{u}} = \mathbf{0} \qquad (2)$$

$$\frac{\partial \tilde{\mathbf{u}}}{\partial \tilde{t}} + \tilde{\mathbf{u}} \cdot \nabla \tilde{\mathbf{u}} = -\nabla \tilde{p} + \frac{Pr^{1/2}}{Ra^{1/2}} \nabla^2 \tilde{\mathbf{u}} + \tilde{T}\hat{\mathbf{g}} \qquad (3)$$

$$\frac{\partial \tilde{T}}{\partial \tilde{t}} + \tilde{\mathbf{u}} \cdot \nabla \tilde{T} = \frac{1}{(RaPr)^{1/2}} \nabla^2 \tilde{T} \qquad (4)$$

The Rayleigh and Prandtl numbers are defined as:

$$Ra = \frac{g\beta T_{ref} H_{ref}^3}{\nu\alpha} \qquad (5)$$

$$Pr = \nu/\alpha \qquad (6)$$

A constant value $Pr = 0.7$ is assumed for air. With reference to Fig. 1, the following non-dimensional boundary conditions are imposed:

$$\tilde{T} = 0, \qquad \tilde{\mathbf{u}} = \mathbf{0} \qquad (7)$$

at the enclosure walls, and:

$$\tilde{T} = 1, \qquad \tilde{\mathbf{u}} = \mathbf{0} \qquad (8)$$

on the cylinder surface.

For the evaluation of the heat transfer rate, the Nusselt number is defined:

$$Nu = \frac{hH_{ref}}{k} \qquad (9)$$

where h represents the average heat transfer coefficient on the source surface.

The numerical technique adopted is based on a Finite Volume implementation of a second order Projection Method, following Gresho (1990). Time-discretizations of the conservation equations are performed according to a three-level scheme, which is fully implicit for the diffusive terms, and explicit Adams-Bashforth for the advective terms. Such a practice is second order accurate in time.

Spatial derivatives are approximated with second order central differences on staggered, non-uniform Cartesian grids. A direct resolution of the discrete momentum and energy equations at each time-step is made possible by means of Approximate Factorization, while the Poisson problem associated with the pressure-velocity coupling (Gresho, 1990) is solved through a fast Poisson solver, based on Matrix Decomposition.

The 2D modelling of arbitrarily irregular boundaries on Cartesian grids is achieved thanks to the original scheme developed by Barozzi *et al.* (2004). The technique involves a local modification of the 5-point computational stencil where boundary segments intersect the stencil arms. The variables on the modified stencil are mapped on the global grid, by means of a linear operator determined by geometrical features and boundary conditions. The overall accuracy of the method is virtually preserved, as well as the computational efficiency of the Cartesian approach.

The Cartesian grids employed are shown in Fig. 2 for each A-value. Along both grid directions, a variable spacing was used, and special care was put on the grid sizing of both near-wall areas and internal domain regions, in view of the work objectives.

As for near-wall zones, the thermal boundary layer thickness was preliminarily estimated by scale analysis. Bejan's estimates (Bejan, 2004) for the heated vertical wall and the heated cylinder were employed, leading to the following expressions:

$$\delta_W \sim \left(\frac{Ra_H}{A}\right)^{-1/4} \qquad (10)$$

$$\delta_S \sim \left(\frac{Ra_H}{A-2}\right)^{-1/4} \qquad (11)$$

As for the internal regions, an approach adopted by Di Piazza and Ciofalo (2000) was used as a criterion to determine the order of magnitude of the maximum cell spacing. Since one of the goals pursued here is to detect the occurrence of non-linear and chaotic dynamical behaviours, the main criterion for the choice of the computational grids is that all relevant (energy-containing) time-dependent flow structures are properly resolved. This requires the mesh size Δx to be of the same order as the Kolmogorov scale Λ_k of dissipative eddies. This can be expressed (Lesieur, 1990) as:

$$\Lambda_k = (\nu^3/\epsilon)^{1/4} \qquad (12)$$

where ϵ is the rate of turbulent kinetic energy dissipation per unit mass. The total dissipation rate of mechanical energy per unit mass in the cavity can be viewed as the product of the buoyancy acceleration, scaling as $g\beta T_{ref}$, by the buoyant velocity, Eq. (1). In fully turbulent flows, *i.e.* in flows presenting high-dimensional chaos, it can be assumed that most of
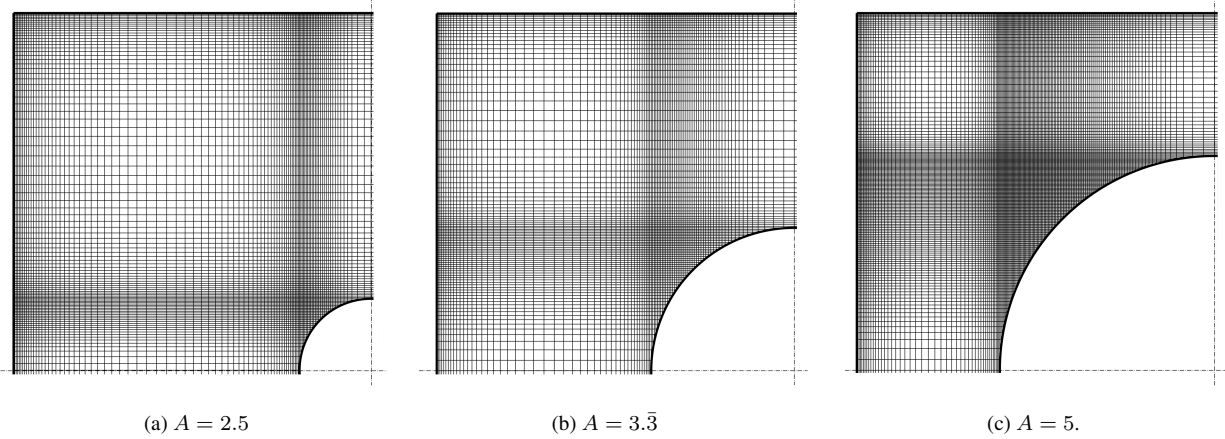
(a) $A = 2.5$ (b) $A = 3.\bar{3}$ (c) $A = 5.$

Fig. 2 Quadrants of the computational grids for each value of the aspect ratio A.

the dissipation occurs through a cascade of turbulent structures. Thus, it is possible to write:

$$\epsilon \approx (g\beta T_{ref})^{3/2} H_{ref}^{1/2} \qquad (13)$$

By substituting Eq. (13) for ϵ into Eq. (12) and taking into account the definition of the Grashof number Gr, the following expression can be derived for the dimensionless dissipative scale $\lambda_k = \Lambda_k / H_{ref}$:

$$\lambda_k \approx Gr^{-3/8} \qquad (14)$$

This is used as an estimate of the maximum dimensionless mesh size $\Delta \tilde{x} = \Delta x / H_{ref}$. Of course, the dissipative scale of thermal structures is of the same order of the scale of the mechanical structures, being the Prandtl number of order unity.

Since, however, the estimate (14) resulted highly conservative for the purposes of the present study, a less restrictive criterion was adopted, following Di Piazza and Ciofalo (2000), who propose a slightly different result for λ_k:

$$\lambda_k \approx (32\pi\sqrt{2})^{1/4} Gr^{-3/8} \qquad (15)$$

based on an alternative definition for the reference velocity U_{ref}. The two estimates, (14) and (15), are the same order of magnitude, and it was assumed that the latter is suitable for the present simulations, either providing enough accuracy and allowing for long-term computations in a relatively short time.

Around the cylinder, the grid spacing follows a cosine distribution. Such a practice is aimed at optimizing the accuracy of the boundary reconstruction method around the circle. A double-sided, constant refinement ratio was then employed to connect the gap zone to the cylinder zone and to the outer walls, as described in Fig. 2. The average grid size in each zone was chosen so as to comply with the criteria described above. The adopted grid sizes for all the A-values are listed in Table 1.

The choice of an implicit scheme for the diffusive terms removes the stability constraint on the time-step width. This remains bound to the Courant-Friedrichs-Levy (CFL) condition, which accounts for the stability of the convective term, treated as explicit. At each cycle, the next

Table 1 Summary of grid sizes adopted and initial Ra_H-values.

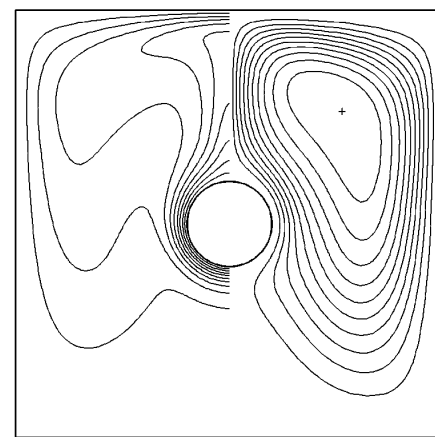| A	grid size	initial Ra_H-value
2.5	190×190	4×10^4
$3.\bar{3}$	188×188	4.2×10^4
5	288×288	1.8×10^4

Fig. 3 Isotherms ($0.1 \leq T \leq 0.9$, left) and streamlines (right) for $Ra_H = 4 \times 10^4$, $A = 2.5$. The (+) sign indicates the maximum for the positive streamfunction.

time-step is computed by calculating the Courant number in each cell:

$$CFL_{i,j} = \frac{\| \tilde{\mathbf{u}}_{i,j}^n \| \Delta \tilde{t}^{n+1}}{\Delta \tilde{x}_{i,j}} \qquad (16)$$

where $\Delta \tilde{t}^{n+1}$ is the $(n+1)$-th time-step, $\Delta \tilde{x}_{i,j}$ the dimensionless cell size, and i, j are the grid indices. The CFL condition implies that:

$$max(CFL_{i,j}) < \xi \qquad (17)$$

where $\xi \leq 1$. $\Delta \tilde{t}^{n+1}$ is extracted from Eq. (16) using condition (17).

For each unsteady simulation the initial conditions were chosen so as to follow the evolution, for increasing Ra_H, of those which had been singled out as the "low-Ra fixed-point solutions" for each A-value. Those solutions correspond to the highest Ra_H-values for which a steady-state, symmetric solution was found by Angeli *et al.* (2008). The corresponding Ra_H values are listed in Table 1. In order to detect the occurrence of bifurcations, Ra_H was increased monotonically from the fixed-point solutions with a constant step $\Delta Ra_H = 2 \times 10^3$, each simulation starting from the final frame of the preceeding one.

All the simulations were protracted to steady-state or, when unsteady flows were detected, until a fixed dimensionless time span was covered. The stop criterion for steady-state was based on the absolute residual r, defined as:

$$r(\phi) = \frac{\sum_{i,j} | \phi_{i,j}^{n+1} - \phi_{i,j}^n | V_{i,j}}{\sum_{i,j} V_{i,j}} \qquad (18)$$

Table 2 Bifurcations of the low-Ra fixed point solution for each A.

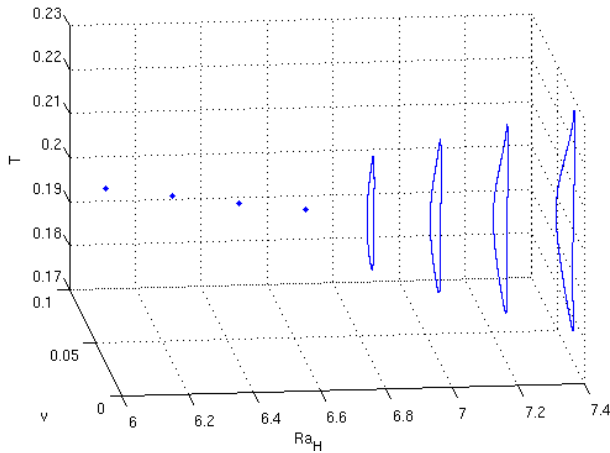| A	$Ra_{H,c}$	*bifurcation type*
2.5	$6.6 \sim 6.8 \times 10^4$	Supercritical Hopf
$3.\bar{3}$	$\approx 9 \times 10^4$	Supercritical Hopf
5	$3.2 \sim 3.4 \times 10^4$	Pitchfork

Fig. 4 Sequence of 2D attractors T-v at point P2, for $A = 2.5$ and for increasing Ra_H.

where ϕ represents the generic variable, and $V_{i,j}$ is the volume of the cell (i, j). Simulations were stopped when the residuals of all variables were less than 10^{-8}.

Supercritical computations for the case $A = 2.5$ have been carried out for four different values of Ra_H, namely for $Ra_H = 1 \times 10^5$, 2×10^5, 4×10^5, 6×10^5. Each of these simulations covered 5×10^3 dimensionless time units. Since the average time-step size in all cases was of order 10^{-3}, it is deduced that the number of integration steps required was of order 10^6. The high efficiency of the numerical method, proved by the extremely low computational time required per time-step (about $100ms$ on a single AMD Opteron®2.4 GHz CPU), allowed such long term simulations to be carried out rather effortlessly.

Time histories of dimensionless temperature, $\tilde{T}$, and velocity components along x and y directions, respectively $\tilde{u}$ and $\tilde{v}$, were tracked for each of the 5 locations indicated in Fig. 1. Values of the variables were interpolated from adjacent cell centers, and time series were resampled with constant time step, in order to use discrete Fourier transforms for time series analysis. Thanks to the degree of spatial and temporal resolution adopted for the discretization, this double resampling operation does not affect data post-processing.

3. RESULTS AND DISCUSSION

The characteristic patterns of the dynamics of the computed temperature and velocity fields are described in this section. For the sake of simplicity, superscripts denoting dimensionless variables will be dropped.

The purposes of the analyses are:

i to observe transitions from a dynamical behaviour to another, *i.e.* the possible occurrence of bifurcations for increasing Ra_H;

ii to identify low-order deterministic sources of the system dynamics and to define their nature (*i.e.* periodic, quasiperiodic or chaotic);

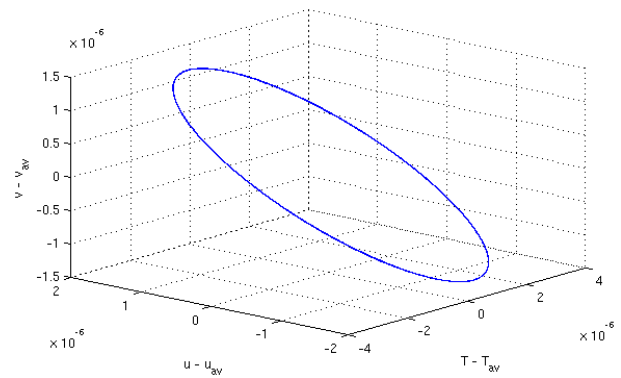iii to clarify the influence of different flow assets on the global heat transfer rate of the system.

Fig. 5 3D attractor in state space T-u-v at point P5, for $A = 3.3$ and $Ra_H = 9 \times 10^4$. The three variables are normalized with respect to their mean values T_{av}, u_{av}, v_{av}.

In view of these goals, and in consideration of the non-linear nature of the underlying phenomena, the representation of the attractors of the computed time series in phase space was chosen as the most appropriate tool for a preliminary morphological analysis. For convenience, attractors are displayed in the three-dimensional state space spanned by the fundamental dependent variables T, u and v.

The analyses have also been supported by Fast Fourier Transform, which is indeed a linear tool but, nonetheless, provides useful elements for a deeper understanding of the system dynamics. Power spectra are reported in linear-log scale with the nondimensional frequency in abscissa, normalized with respect to a reference resampling frequency $f_{ref} = 1/64$.

3.1. First bifurcations of low-Ra solutions

Table 2 summarizes the results of the solution-following procedure outlined in the previous section. By increasing Ra_H with a constant step, for each A-value, an unstable behaviour of the corresponding low-Ra fixed-point solution was observed. The features of such instabilities and their relationship with the underlying bifurcations are discussed.

For $A = 2.5$, the base solution at $Ra_H = 4 \times 10^4$ consists in a steady-state flow characterised by two counter-rotating, symmetric vortices raising a thermal plume above the cylinder (Fig. 3). The system reaches the asymptotical fixed-point monotonically for $Ra_H < 5 \times 10^4$. If Ra_H is increased further, the approach to steady-state is characterised by a weak, exponentially damped oscillation, the asymptotical decay time of the oscillation increasing with Ra_H. As Ra_H is increased from $Ra_H = 6.6 \times 10^4$ to $Ra_H = 6.8 \times 10^4$, the oscillation starts to amplify, until a periodic limit cycle is reached. In Fig. 4, 2D projections of the corresponding T-u-v attractors are plotted as a function of Ra_H. The passage from the lower-Ra fixed-point solution to the periodic orbit is clearly portrayed, thus suggesting the occurrence of a Supercritical Hopf bifurcation, with a critical value of the Rayleigh number $Ra_{H,c} = 6.6 \sim 6.8 \times 10^4$.

The system behaviour for $A = 3.\bar{3}$ is identical, except for the higher value of $Ra_{H,c}$. Such a shift in the occurrence of the Hopf bifurcation had already been roughly predicted by Angeli *et al.* (2008), who observed a periodic flow for $Ra_H = 2.11 \times 10^5$. Here, the critical value $Ra_{H,c}$ could be determined with better accuracy, and was estimated to be very close to $Ra_{H,c} = 9 \times 10^4$. For that Ra_H-value, the system was found to approach a limit cycle characterised by an oscillation amplitude of order 10^{-6}. The corresponding T-u-v attractor is shown in Fig. 5, where the three variables are normalized with respect to their mean values, in order to appreciate the order of magnitude of the orbit radius. The observation of such a small-amplitude limit cycle confirms the supercritical nature of the Hopf bifurcation.
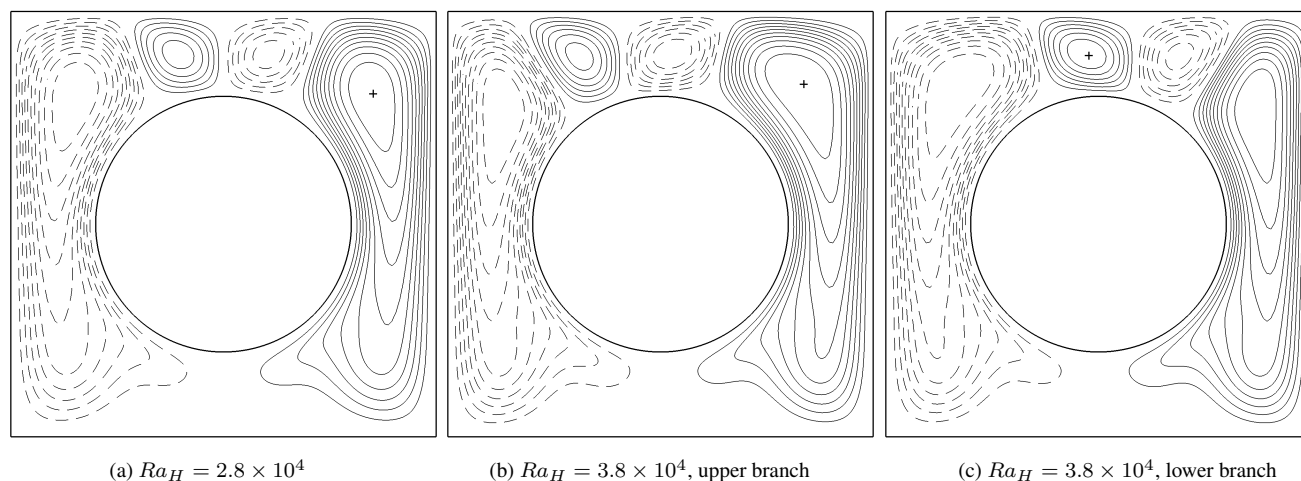
(a) $Ra_H = 2.8 \times 10^4$ (b) $Ra_H = 3.8 \times 10^4$, upper branch   (c) $Ra_H = 3.8 \times 10^4$, lower branch

Fig. 6 Streamlines for different fixed-point solutions for the case $A = 5$: (a) symmetric flow field; (b) and (c) dual non-symmetric fields. The (+) sign indicates the maximum for the positive streamfunction.
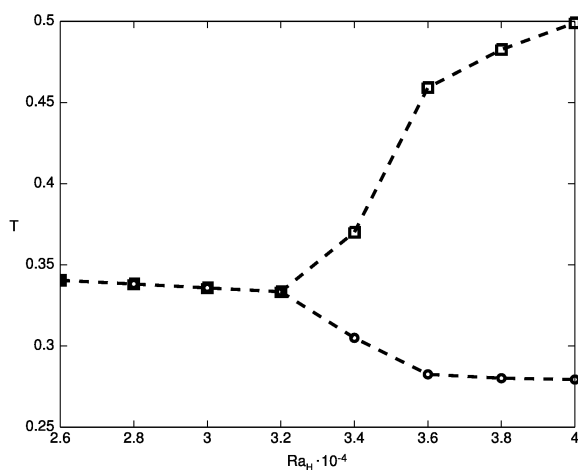

Fig. 7 Bifurcation diagram of the dimensionless temperature at point P4 vs. Ra_H, $A = 5$. (□) and (○) symbols refer to the two branches associated with the two non-symmetric mirrored solutions.

Fig. 8 Instantaneous temperature field at $\tilde{t} = 5 \times 10^3$ for $A = 2.5, Ra_H = 2 \times 10^5$.

For the highest value of the aspect ratio A considered, $A = 5$, the behaviour radically changes, starting from the low-Ra base-solution. As shown in Fig. 6(a), aside the main circulations characterising the flow field for $A = 2.5$ and $A = 3.\bar{3}$, two small counter-rotating secondary cells appear. The reduced space strengthens the inverse thermal gradient established across the gap above the cylinder top, thus giving rise to the formation of these Rayleigh-Bénard-type rolls.

As Ra_H is increased beyond $Ra_H = 3.2 \times 10^4$, the asymptotic solution is still a fixed-point, but the flow and thermal fields appear as non-symmetric, see Fig. 6(b). This symmetry-breaking pattern is typical of pitchfork bifurcations, and is not uncommon in confined buoyant flows (Desrayaud and Lauriat, 1998). The occurrence of a pitchfork bifurcation is confirmed by the existence of a stable mirrored dual solution, as shown in Fig. 6(c), for each of the non-symmetric configurations. The diagram of Fig. 7, representing the dimensionless temperature T at point P4 as a function of Ra_H, clearly shows the separation of the two solution branches past the bifurcation point. The critical Ra_H value can be located in the interval $Ra_{H,c} = 3.2 \sim 3.4 \times 10^4$.
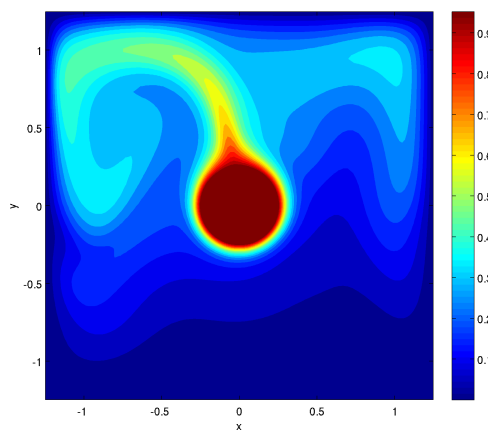
3.2. Supercritical behaviour for A = 2.5

An additional set of computations was performed for the case $A = 2.5$, in order to trace a general picture of the system evolution beyond the Hopf bifurcation described above.

Figure 8 shows an instantaneous snapshot of the temperature field for the condition $Ra_H = 2 \times 10^5$, indicating the persistence of a regular thermal plume above the cylinder. Such a feature is common to all the cases investigated for $A = 2.5$.

In order to describe the evolution of the system dynamics with increasing Ra_H, power spectral densities of variables T-u-v at point P1 are shown in Fig. 9, while Fig. 10 reports the attractors plotted in the T-u-v state space for the system dynamics observed at point P1 (on the left-hand column) and P3 (on the right-hand column), for four increasing values of Ra_H.

The system dynamics for $Ra_H = 1 \times 10^5$ can be again identified as periodic. The numerical attractors in points P1 and P3 (displayed in Fig. 10(a)) show the existence of a well defined and closed limit cycle, which can be assumed to represent the high amplitude-low frequency dynamical patterns typical of the swaying oscillation of buoyant plumes (Desrayaud and Lauriat, 1998) with respect to the vertical symmetry axis. This periodic nature is confirmed by the analysis in the frequency domain.
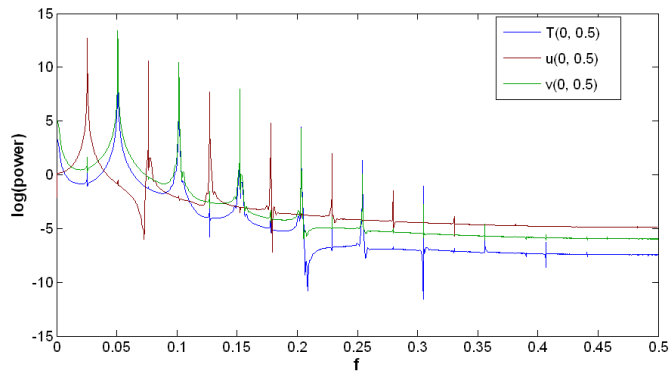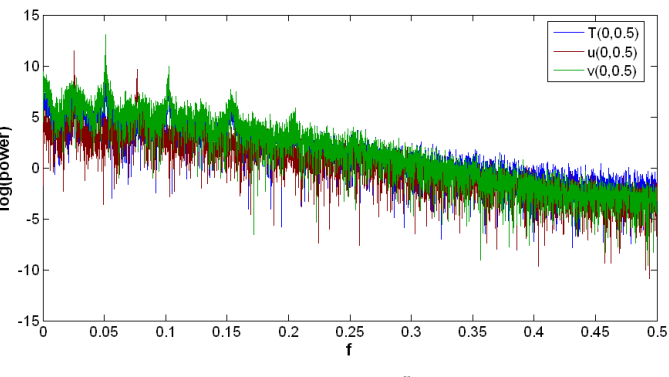
(a) $Ra_H = 1 \times 10^5$
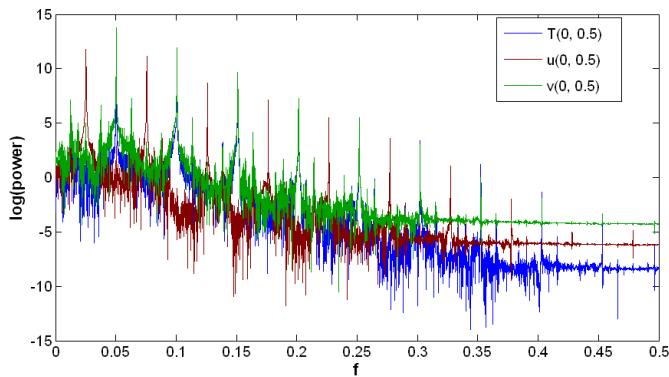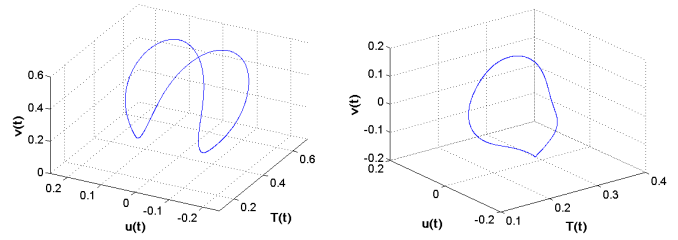

(b) $Ra_H = 2 \times 10^5$
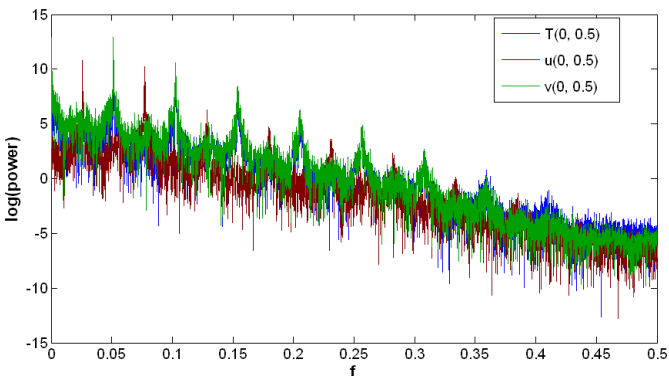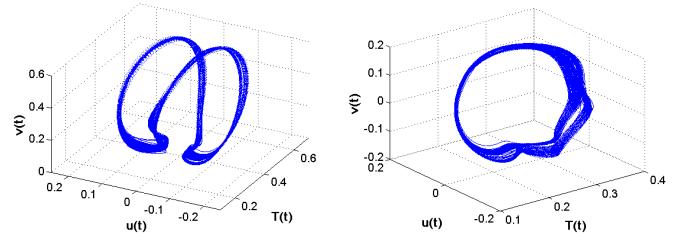

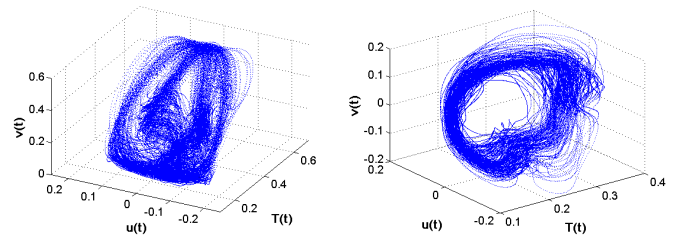(c) $Ra_H = 4 \times 10^5$

(d) $Ra_H = 6 \times 10^5$

Fig. 9 Power spectral densities of state variables T-u-v at point P1 for increasing Ra_H-values.
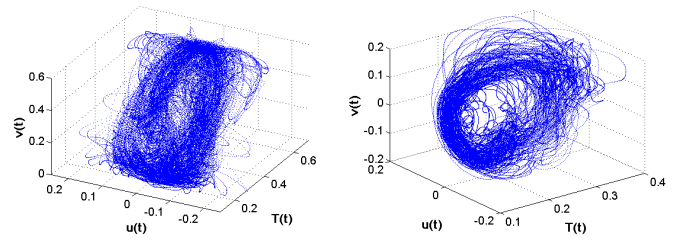

(a) $Ra_H = 1 \times 10^5$

(b) $Ra_H = 2 \times 10^5$

(c) $Ra_H = 4 \times 10^5$

(d) $Ra_H = 6 \times 10^5$

Fig. 10 3D attractors in state space T-u-v at: point P1 (left) and point P3 (right) for increasing Ra_H-values.

In fact, power spectra of variables T, u and v at point P1, displayed in Fig. 9(a), show a typical periodic behaviour. It is possible to observe that the spectra of T and v appear almost overlapped in the low frequency range, where the dominant dynamical features are contained; this is in fair accordance with the observation of almost parallel trajectories describing the corresponding limit cycle in state space T-u-v, as reported in Fig. 10(a), left-hand plot. On the other hand, the power spectrum of the horizontal velocity u at point P1 is characterised by a lower dominant frequency, with respect to the other two variables; this means that the pulsation of the plume in the horizontal direction represents indeed the main dominant pattern, from a dynamical standpoint. Moreover, the dynamics of the three variables being interrelated, harmonics and sub-harmonics of the dominant frequencies detected in power spectra are reciprocally bound by rational ratios.

The effect of the increase of Ra_H can be observed by spanning Figures 9 and 10. In particular, it can be inferred that the periodic flow detected for $Ra_H = 1 \times 10^5$, and illustrated in Fig. 10(a), undergoes a series of bifurcations that lead to a chaotic flow at $Ra_H = 2 \times 10^5$.

By comparing Fig. 9(a) and Fig. 9(b), it is possible to observe a broadening of the range of excited frequencies in the power spectra of the
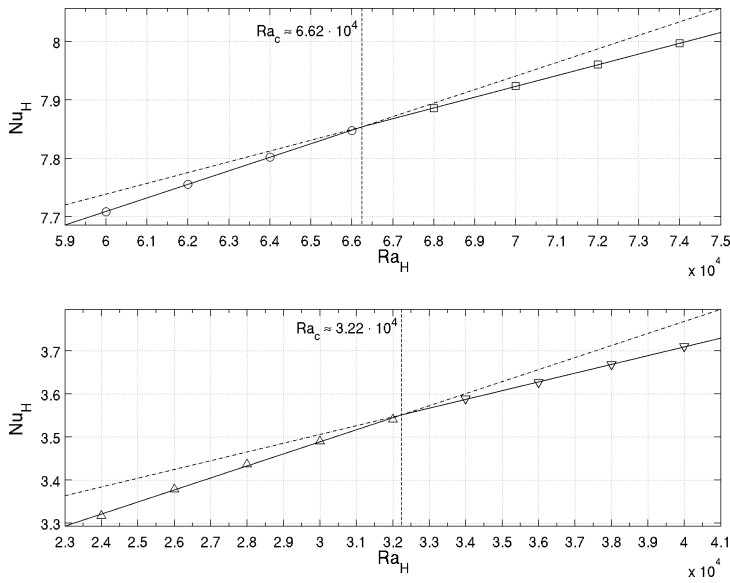
Fig. 11 Average Nu_H on the cylinder surface vs. Ra_H around the first bifurcation points for $A = 2.5$ (top) and $A = 5$ (bottom).

Fig. 12 Heat transfer results for all the sub- and supercritical cases investigated, for $A = 2.5$ and $A = 5$, as compared with Eq. (19).

three variables, where, nevertheless, dominant features can be still singled out. This is due to the rise of frequency bands, typical of chaotic dynamics. The attractors displayed in Fig. 10(b) plots show a well defined morphology. The general shape of the attractors is clearly resemblant to that observed for the case $Ra_H = 1 \times 10^5$, but the remarkable fractal structure displayed by a folded band nature of the attractors themselves indicates the presence of a source of low-order chaos.

The numerical attractors as well as the power spectra obtained for $Ra_H = 4 \times 10^5$ show the appearance of higher order effects in the system dynamics. The frequency peaks in the power spectrum (Fig. 9(c)) appear less distinguishable, and the attractors' morphology Fig. 10(c)) is affected by a noticeable spreading of the trajectories, determining an enlargement of the phase space region occupied by the attractor itself (*i.e.* of the attractor global dimension).

Finally, the case $Ra_H = 6 \times 10^5$ is characterised by a broadband power spectrum (Fig. 9(d)), where the frequency bands of the quasi-periodic flow can hardly be distinguished from the "noisy" background. Although traces of the original attractor shapes are still visible (Figures 10d), the trajectories are diffusely spread over the phase-space region, indicating high-order dynamics as a prominent feature of the asymptotical system behaviour.

As a general consideration on the effect of the increase of Ra_H, it is worth observing that for all of the cases examined, the general morphology of the attractor clearly appears as an evolution of the periodic case observed for $Ra_H = 1 \times 10^5$, although the originally stable limit cycle becomes unstable, giving way to the birth of chaotic behaviours characterised by dynamical effects of increasing order.

The issue of flow transition and bifurcations for the present geometry has never been discussed in depth so far, although the occurrence of a number of non-linear effects has already been reported by Angeli *et al.* (2008). Very little feedback on the reliability of the present results can therefore be gained from the literature, however, it is important to note that some of the elements of the overall scenario depicted so far stand in satisfactory agreement with the results reported by Desrayaud and Lauriat (1998) for the case of very small cylinders and horizontal line heat sources in air-filled rectangular vessels with adiabatic sides and isothermal horizontal walls. For that case, they detected a supercritical Hopf bifurcation for $Ra_L = 1.5 \sim 1.6 \times 10^6$, which corresponds to $Ra_H = 1.875 \sim 2 \times 10^5$. Such values compare favourably with the
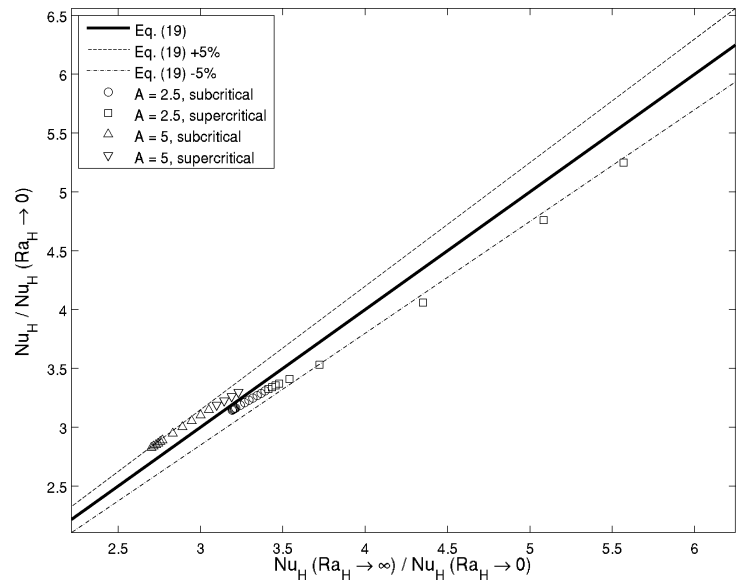
critical range $Ra_{H,c} = 6.6 \sim 6.8 \times 10^4$ established here for $A = 2.5$, in view of the significant differences in the source size and the thermal boundary conditions at the enclosure and the cylinder walls. Moreover, the supercritical scenario reported by Desrayaud and Lauriat (1998) is analogous to the one described here, thus corroborating the validity of the present results.

3.3. Heat transfer

The effect of the observed bifurcations on the global heat transfer rate of the system is briefly discussed. Fig. 11 shows the average Nusselt number on the cylinder surface, as a function of Ra_H, around the bifurcation points detected for $A = 2.5$ and $A = 5$. Power-law least-squares fittings of the sub- and supercritical heat transfer data are plotted alongside the predicted data. In both cases, it is seen that transition affects the $Nu_H - Ra_H$ dependence, resulting in a reduction of the growth rate of Nu_H with Ra_H past the bifurcation point. This suggests the possibility of extrapolating closer guess of the critical Rayleigh number $Ra_{H,c}$ by the intersection of the two trendlines, as indicated in the graphs. For the two cases considered, the result is $Ra_{H,c} \simeq 6.62 \times 10^4$ for $A = 2.5$, and $Ra_{H,c} \simeq 3.22 \times 10^4$ for $A = 5$

All the heat transfer data collected for the cases $A = 2.5$ and $A = 5$ are also plotted in Fig. 12, in normalized coordinates, and compared with the general correlation obtained by Angeli *et al.* (2008), for the subcritical range ($Ra_H \leq 2 \times 10^4$) and for a wider range of A-values ($2.5 \leq A \leq 10$). In terms of the (Ra_H, A) parameters, the correlation reads as follows:

$$Nu_H(Ra_H, A) = \left\{ \left[0.54 + \frac{1.178}{(A-2)^{0.637}} \right]^{14} + \left[\left(0.15 + \frac{0.256}{A-2} \right) Ra_H^{\left(0.265 + \frac{0.02}{A-2} \right)} \right]^{14} \right\}^{\frac{1}{14}} \quad (19)$$

As shown in Fig. 12, the present predictions, either sub- or supercritical, all fall within the $\pm 5\%$ accuracy strip of Eq. (19), except for those corresponding to the highest Ra_H-values, for $A = 2.5$. The validity of the correlation can therefore be safely extended to the supercritical region, at least for $Ra_H \leq 2 \times 10^5$, $A = 2.5$ and $Ra_H \leq 4 \times 10^4$, $A = 5$.

4. CONCLUDING REMARKS

Transitional natural convection flow regimes, arising from a horizontal cylindrical source centred in an air filled cavity of square cross-section, were investigated numerically. Three values of the aspect ratio A were considered, for which the nature of the first bifurcations of the low-Ra fixed point solution, and the related critical Rayleigh number values were determined.

It is observed that, for the two lower A-values, the dynamics of transition are governed by the thermal plume arising from the cylindrical source, and Hopf bifurcations appear as the first sign of flow transition. For the highest value of the parameter, the flow asset is primarily influenced by the formation of Rayleigh-Bénard-type rolls above the heat source. These structures undergo pitchfork bifurcations, as detectable by the appearance of co-existing, mirrored non-symmetric fixed-point solutions.

Additional computations were performed for the case $A = 2.5$ and four values of the Rayleigh number well beyond the critical value of the first Hopf bifurcation, to provide a general picture of the successive transitions leading to the onset of chaotic flow. Time series were analyzed by means of phase space representations and power spectra, revealing the occurrence of non-linear dynamical patterns in the asymptotic behaviour of the system. Specifically, a periodic limit cycle was detected for the lowest value of Ra_H considered, and low-order chaos was observed for the second one, evidenced by the fractal structure of the attractors in phase space.

Finally, the analysis of global heat transfer data showed that the $Nu_H - Ra_H$-relationship is sensibly influenced by the transition mode associated with each A-value. A correlating equation for the average Nusselt number on the cylinder, derived for the subcritical case, was found to be valid up to slightly supercritical Ra_H-values.

ACKNOWLEDGMENTS

The authors would like to dedicate this work to the memory of Prof. Gilles Desrayaud.

NOMENCLATURE

A	aspect ratio
D	cylinder diameter (m)
CFL	Courant number
f	frequency (Hz)
f_{ref}	reference resampling frequency $(n_{samples}^{-1})$
h	average heat transfer coefficient $(W/(m^2 K))$
H	vertical gap (m)
k	thermal conductivity $(W/(mK))$
L	enclosure side length (m)
$n_{samples}$	number of samples
Nu	Nusselt number
p	pressure (Pa)
Pr	Prandtl number
r	residual
Ra	Rayleigh number
t	time (s)
T	temperature (K)
T_{ref}	reference temperature (K)
$\mathbf{u}$	velocity vector (m/s)
U	velocity modulus (m/s)
x, y, z	Cartesian coordinates (m)

Greek Symbols

α	thermal diffusivity (m^2/s)
β	thermal expansion coefficient $(1/K)$
ϵ	turbulent kinetic energy dissipation rate (m^2/s^3)
ν	kinematic viscosity (m^2/s)
λ	dimensionless length scale
Λ	length scale (m)
τ	CPU time per time-step
ϕ	general variable
ξ	CFL threshold

Superscripts

$\tilde{}$	dimensionless variable

Subscripts

av	average
c	critical
H	gap
i, j	grid indices
K	Kolmogorov
ref	reference
S	source
W	wall

REFERENCES

Angeli, D., Barozzi, G.S., Collins, M.W., and Kamiyo, O.M., 2010, "A critical review of buoyancy-induced flow transitions in horizontal annuli," *International Journal of Thermal Sciences*, **49**, 2231–2492, doi:10.1016/j.ijthermalsci.2010.08.002.

Angeli, D., Levoni, P., and Barozzi, G.S., 2008, "Numerical predictions for stable buoyant regimes within a square cavity containing a heated horizontal cylinder," *International Journal of Heat and Mass Transfer*, **51**, 553–565, doi:10.1016/j.ijheatmasstransfer.2007.05.007.

Barozzi, G.S., Bussi, C., and Corticelli, M.A., 2004, "A fast cartesian scheme for unsteady heat diffusion on irregular domains," *Numerical Heat Transfer B*, **46**, 56–77, doi:10.1080/10407790490430642.

Bejan, A., 2004, *Convection Heat Transfer*, 3rd ed., John Wiley & Sons.

Desrayaud, G., Fichera, A., Marcoux, M., and Pagano, A., 2006, "An analytical solution for the stationary behaviour of binary mixtures and pure fluids in a horizontal annular cavity," *International Journal of Heat and Mass Transfer*, **49**, 3253–3263, doi:10.1016/j.ijheatmasstransfer.2006.02.002.

Desrayaud, G., and Lauriat, G., 1998, "Unsteady confined buoyant plumes," *Journal of Fluid Mechanics*, **252**, 617–646, doi:10.1017/S002211209300391X.

Di Piazza, I., and Ciofalo, M., 2000, "Low-Prandtl number natural convection in volumetrically heated rectangular enclosures: I. Slender cavity, AR = 4," *International Journal of Heat and Mass Transfer*, **43**, 3027–3051, doi:10.1016/S0017-9310(99)00365-8.

Gresho, P.M., 1990, "On the Theory of Semi-Implicit Projection Methods for Incompressible Flow and its Implementation via a Finite Element Method that also introduces a Nearly Consistent Mass Matrix. Part 1: Theory," *International Journal for Numerical Methods in Fluids*, **11**, 587–620, doi:10.1002/fld.1650110509.

Hewitt, G.F., editor, 1992, *Handbook of Heat Exchanger Design*, Begell House.

Lesieur, M., 1990, *Turbulence in Fluids*, Kluwer Academic Publisher.

Mack, L.R., and Bishop, E.H., 1968, "Natural convection between horizontal concentric cylinders for low Rayleigh numbers," *Quarterly Journal of Mechanics and Applied Mathematics*, **21**, 223–241, doi:10.1093/qjmam/21.2.223.

Mojtabi, A., and Caltagirone, J.P., 1979, "Étude de la stabilité d'un écoulement de convection naturelle dans un espace annulaire horizontal," *Journal de Mécanique*, **18**, 225–241.

Teertstra, P., and Yovanovich, M.M., 1998, "Comprehensive review of natural convection in horizontal circular annuli," *Seventh* AIAA/ASME *joint Thermophysics and Heat Transfer Conference*, vol. 357 of ASME-HTD, 141–152.

Warrington, J.R.O., and Powe, R.E., 1985, "The transfer of heat by natural convection between bodies and their enclosures," *International Journal of Heat and Mass Transfer*, **28**, 319–330, doi:10.1016/0017-9310(85)90065-1.